Pseudo-Three-Dimensional Analytical Model of Linear Induction Motors for High-Speed Applications

Simone Rametti, *Student Member, IEEE,* Lucien Pierrejean, André Hodder, *Senior Member, IEEE,*
and Mario Paolone, *Fellow, IEEE*

Abstract—Literature on linear induction motors (LIMs) has proposed several approaches to model the behavior of such devices for different applications. In terms of accuracy and fidelity, field analysis-based models are the most relevant. Closed-form or numerical solutions can be derived, based on the complexity of the model and the underlying hypotheses. In terms of simplicity, equivalent circuit-based models are the most effective, since they can be easily integrated into optimization frameworks. To the best of the authors' knowledge, the literature has not yet provided a computationally efficient LIM analytical model that considers the main characteristics of this type of motor altogether (i.e. finite motor length, magnetomotive force (mmf) space harmonics, slot effect, edge effect, and tail effect) and that is numerically and experimentally validated, especially at high speed (i.e. $v \simeq 100\,\mathrm{m\,s^{-1}}$). Within this context, this paper proposes a field analysis-based pseudo-three-dimensional model of LIMs that explicitly takes into account the above-mentioned effects. The derived closed-form solution makes the model computationally more effective than traditional f.e.m. models and, therefore, suitable to be coupled with optimization frameworks for optimal LIM design. The performance and accuracy of the proposed model are assessed through numerical simulations and experimental measurements, carried out by means of a dedicated test bench.

Index Terms—Linear induction motors, Transportation, Magnetic vector potentials, Magnetic levitation, Modeling.

I. INTRODUCTION

LINEAR induction motors (LIMs) have been known for a long time, especially in industrial applications requiring linear actuation [1]. Although not commonly used, they have been intensively studied for high-speed (i.e. $v \simeq 100\,\mathrm{m\,s^{-1}}$) transportation applications [2]–[8]. A possible transportation application where LIMs are considered to be a potential candidate for the propulsion system is the Hyperloop [9]–[11]. As known, the Hyperloop concept envisages near-sonic speed transportation of people or freights, realized through capsules propelled by energy-efficient systems, into partially depressurized infrastructures, with the main goal of disrupting intra-continental flights by increasing the energy efficiency of long-distance journeys [12]. LIMs have recently regained attention from the scientific community for such types of applications mainly because of their construction simplicity, infrastructure

passivity (i.e. rails do not need to be electrified or magnetized), contact-less thrust and levitation force generation [5]. However, due to: (i) the inherently large air gap necessary to guarantee the safety of the capsule at high speed, (ii) the effect of finite motor length on the developed thrust, (iii) the non-magnetic reaction rail, the efficiency and power factor of such electrical machines are considerably lower than the traditional rotating counterparts. Proper mathematical models and optimization frameworks are therefore fundamental for the optimal design of these devices since they allow to determine the configurations that maximize certain metrics, such as thrust density, lift density, power factor, or a combination of them [13].

Current literature on LIM models has proposed several modeling approaches that can be categorized into: 1) field analysis-based models, whose governing equations can be either solved numerically (f.e.m.) or via closed-form solutions with adequate hypotheses (analytical), and 2) equivalent circuit-based models. Field analysis-based models with closed-form solutions are the most appealing from the authors' point of view because they allow to accurately model most LIM characteristics while reducing the computational complexity compared to numerical solutions (f.e.m.-based). To the best of the authors' knowledge, the vast majority of field analysis-based models with closed-form solutions found in the literature use Fourier series decomposition methods to solve the governing differential equations [7], [14], [15]. One of the main hypotheses of such an approach is the assumption of a constant air gap along the entire domain (i.e. even outside the LIM edges), which implies an infinite primary length with the windings distributed along a limited section [16], [17]. Because of this hypothesis, the magnitude of the electromagnetic fields computed at the motor's rear is higher than reality (see Fig. 1), and, therefore, the computed LIM longitudinal and normal forces are overestimated. The error of the calculated forces becomes significantly relevant as speed increases and can reach values of 40% or more for speed of $20\,\mathrm{m\,s^{-1}}$, as shown in [17].

Moreover, to the best of the authors' knowledge, the literature on LIMs lacks computationally efficient models that are experimentally validated at high speed ($v \simeq 100\,\mathrm{m\,s^{-1}}$). To overcome these limits, this work proposes a pseudo-three-dimensional field analysis-based model of a double-sided linear induction motor (DSLIM) where the field-based differential equations have been solved analytically by imposing
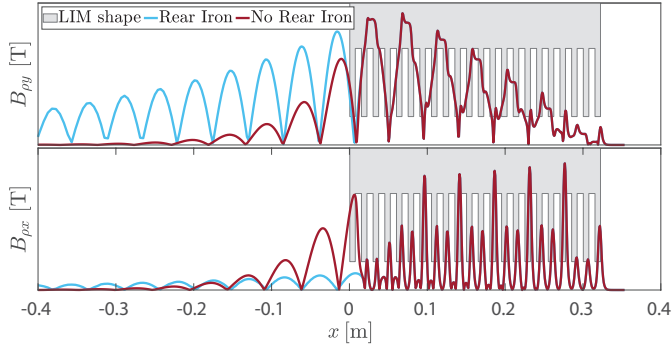
Fig. 1. Effect of the infinite iron at the LIM rear on the magnetic flux density. COMSOL f.e.m. simulation: Pair of poles: 3, $\tau_p = 4.5\,\text{cm}$, Number of slots per pole per phase (NSPP): 1, $\delta = 3.5\,\text{mm}$, $\epsilon = 2\,\text{mm}$, $v_m = 120\,\text{m s}^{-1}$, $f_s = 1323\,\text{Hz}$. See Section III for parameters description.

proper modeling assumptions. The proposed model explicitly considers the following characteristics altogether:

- Finite motor length (extremity effect).
- Finite motor width (edge effect).
- Windings harmonics.
- Slots effect.
- Effect of the electromagnetic fields at the rear of the motor (hereafter referred to as tail effect).

The presented model proves to be largely more efficient in terms of computation complexity than f.e.m. simulations, and has been numerically and experimentally validated through comparison with f.e.m. simulations and measurements using a custom-made test bench capable of reaching speeds up to $100\,\text{m s}^{-1}$. The paper is structured as follows: Section II discusses the state of the art on LIMs modeling and lists the work contributions. It describes the main related works found in literature, their advantages, and their disadvantages. Section III describes the proposed model of a DSLIM, starting from framework definition, hypotheses, differential equations formulation, and solution. Section IV presents the numerical and experimental validation of the model through comparisons with f.e.m. models and measurements carried out on a custom-made test bench. Section V summarises the proposed analytical model and the results of the numerical and experimental validation.

II. STATE OF THE ART

This section presents the main works on LIMs modeling existing in the current literature. The section is divided into two main subsections, one per model category, as done in the paper introduction.

A. Field analysis-based models

Field analysis-based models can be divided into two sub-categories based on the methods used to solve the differential equations governing the system.

1) Analytical models: Among all field analysis-based models of LIMs, the ones based on the direct solution of field equations are the oldest. One of the main advantages of such models is the phenomenological understanding of the system, since the solutions are directly derived from fundamental electromagnetic differential equations suitably coupled with hypotheses that allow for the analytical integration [4]. Most of the models found in the literature are 1D (i.e. fields vary in one direction only) or 2D, where effects such as finite motor height along the transverse direction or slots effect on the field distribution are considered by applying correction coefficients or not considered at all [4], [5].

The authors of [16], [18], [19] propose one-dimensional and two-dimensional models of DSLIMs operating at very high speed (i.e. $v \simeq 150\,\text{m s}^{-1}$). In [18] particular focus is on extremity effect[1] and ways to compensate for it. Despite their clarity in the explanation of the extremity effect, these models ignore the effect of slots/teeth alternation in the air gap and the magnetomotive force (mmf) harmonics introduced by windings. A pseudo-3D derivation is performed by adding a correction factor to the reaction rail conductivity.

The slots effect, i.e. the effect of slots and teeth alternation on the air gap field distribution is approximated in [5], [20] by using Carter's coefficient to derive the expression of the equivalent air gap [21]. In both models, the primary winding current is decomposed into a sum of its harmonics. Such an approach allows to include the effect of winding harmonics on the developed thrust. The transverse edge effect and slot effect are approximated by introducing correction coefficients.

Closed-form solution of the magnetic vector potential for a single-sided LIM is derived in [15], [17] through a Fourier series decomposition method. In [17] the LIM winding is modeled as a distribution of infinitely long wires carrying current and the solution of the magnetic vector potential in the reaction rail and in the air gap is derived by imposing boundary conditions on the electromagnetic fields (i.e. continuity of both the magnetic flux density normal component and the magnetic field tangential component). Although the derived model is simple and computationally efficient, the assumptions of slot-less and constant air gap along the entire Fourier series period imply large errors in the computed thrust and lift (up to 40% at $20\,\text{m s}^{-1}$) compared to f.e.m. models, which increase significantly at high speed.

2) Finite element method-based models: F.e.m. is definitely the most recently adopted technique for electrical motor modeling since the numerical solution of the system's differential equations allows to attain a high-fidelity analysis with no approximation of the underlying physics. In the field of LIMs design, the need for f.e.m. is justified by the complexity of the system, whose effects (e.g. skin effect in the reaction rail, flux leakages) cannot be entirely considered through an exact analytical formulation.

The authors of [22] propose a complete 3D f.e.m. model of

---

[1]Extremity effect is the direct consequence of finite motor length and it leads to magnetic field perturbations at the motor entry, due to the incoming reaction rail. This phenomenon is therefore responsible for the LIMs performance degradation (i.e. thrust and efficiency), particularly relevant at high speed.

a LIM with particular attention to thrust calculation. However, since the computation time to solve these models is extremely high (e.g. between 74 and 120 hours for a time domain simulation of 2 pairs of poles LIM with approximately 250000 mesh elements [22]), such a technique cannot be efficiently integrated into an optimization framework with a multi-dimensional solution space.

The authors of [23] propose a novel method to identify an equivalent electrical circuit of a tubular LIM from f.e.m. models, for both static and dynamic operating conditions. This type of approach can be used to analyze the motor characteristics once the design has been already fixed.

Peculiar LIM arrangements, such as double-stator LIMs, are easily analyzed through f.e.m. models, as proposed in [24] where the authors investigate the coupling effect of a double-stator LIM with respect to the supply connection type of the two parts.

The effect of the stator winding arrangement on the magnetic flux density is studied in [25]. The authors use f.e.m. models to assess which winding arrangement is the best option in terms of magnetic flux density maximization for Maglev transportation applications.

As emerged from the literature review, f.e.m. is a more useful method for a-posteriori analysis rather than design optimization because of its high computation complexity and, therefore, simulation time.

B. Equivalent circuit models

Equivalent circuit-based models (ECMs) are the most common models in the literature and practical applications. Because of their simplicity, ECMs are useful models that can be integrated into control system simulations, dynamic motor simulations, and design-oriented optimization problems, where metrics such as power factor, efficiency, thrust, or a combination of them are the objective functions, as described in [13]. However, it is not always possible to correctly account for every effect of a LIM through this type of model, and, therefore, several hypotheses have to be made to simplify the analysis (e.g. three-phase supply, sinusoidal distribution of air gap mmf, slot-less primary,...).

Duncan proposes an equivalent circuit based on traditional rotating induction machine circuits [26]. The extremity effect is accounted for by introducing a dimensionless coefficient that models the reduction of thrust with the increase of the velocity. Duncan's model has been lately improved in [27] by adding the expression of the reaction rail leakage inductance. Alternatively, [28] provides a T-model equivalent circuit of single-side LIMs where the longitudinal extremity effect and the transversal edge effect are taken into account through compensation coefficients derived from the magnetic vector potential differential equation solved in the air gap. The proposed ECM neglects the effect of the primary slots and the space harmonics introduced by the winding configuration and has been experimentally validated at relatively low speed (i.e. up to $12\,\mathrm{m\,s^{-1}}$).

Core losses and flux leakages in the primary iron can be modeled via dedicated magnetic equivalent circuit models,

similarly to what is done in [29], [30]. Although these ECMs are conceived for rotating induction machines, they can be adapted to their linear counterparts. However, the computation of the LIM transverse force, which is fundamental for applications that target the lift of payloads, is only possible by using a field analysis-based model, which is the approach the proposed model relies on.

C. Paper's contribution

This paper proposes a computationally efficient pseudo-three-dimensional analytical model of a DSLIM where the magnetic vector potential differential equations have been solved through a complex Fourier series decomposition method. The model groups together the main characteristics of LIMs found in literature and extends the validity of the results to high speeds (i.e. $v \simeq 100\,\mathrm{m\,s^{-1}}$). In particular, it proposes a compensation related to the effect of the hypotheses of slot-less and constant air gap (typical for all analytical models solved through Fourier series decomposition methods [5], [17], [20]). The validation of the proposed model through comparisons with f.e.m. and experimental measurements is carried out and presented.

III. ANALYTICAL MODEL DESCRIPTION

A. Model geometry

The proposed DSLIM model takes inspiration from [17] for the resolution of the system's differential equations. Fig. 2 shows the reference frame of the model as well as the realistic geometry of half DSLIM. According to the hypotheses listed hereafter, the model refers to the simplified DSLIM geometry shown in Fig. 3a. However, the compensation for some of the simplifications introduced by the hypotheses, as presented later, will bridge the gap between the simplified and the realistic model.

The direction of movement is along the $\hat{\mathbf{x}}$ axis and the winding conductors are along the $\hat{\mathbf{z}}$ axis only, and so is the magnetic vector potential $\vec{A} = A_z(x,y)\hat{\mathbf{z}}$. In steady state, the magnetic vector potential $A_z(x,y)$ in the air gap and in the reaction rail can be described by a single differential equation [31], [32]:

$$\nabla^2 A_z(x,y) = \mu\sigma \left(j\omega A_z(x,y) - v_m \frac{\partial A_z(x,y)}{\partial x} \right) \quad (1)$$

where $A_z(x,y)$ is the magnetic vector potential $\hat{\mathbf{z}}$ component, v_m is the LIM velocity, μ and σ are the magnetic permeability and conductivity of the considered medium. This differential
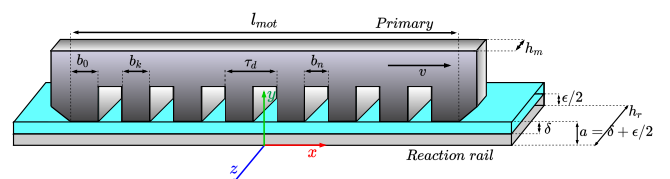

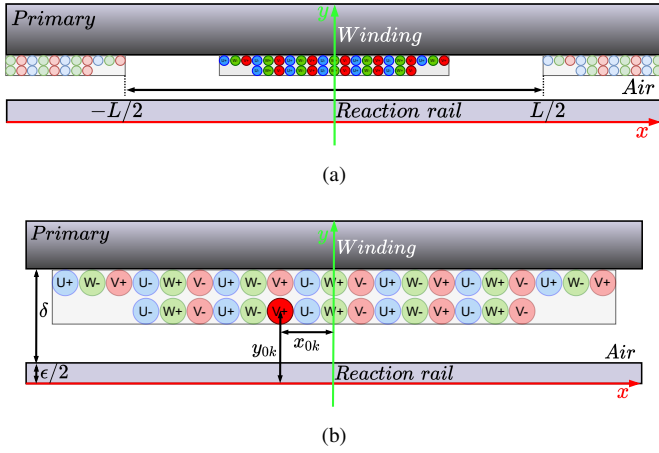Fig. 2. Realistic half-DSLIM geometry and reference frame.

Fig. 3. Simplified half-LIM geometry. (a) Fourier series representation. (b) Winding detail.

equation is valid in general and will be solved in three different regions, denoted by the following notation:

1: Primary $\qquad y \geq \delta + \dfrac{\epsilon}{2} \to A_z(x,y) = A_{\mu z}(x,y)$

2: Air gap $\qquad \dfrac{\epsilon}{2} \leq y \leq \delta + \dfrac{\epsilon}{2} \to A_z(x,y) = A_{\delta z}(x,y)$

3: Reaction rail $\qquad 0 \leq y \leq \dfrac{\epsilon}{2} \to A_z(x,y) = A_{\rho z}(x,y)$

B. Model hypotheses

1) Primary iron dimensions along $\hat{x}$ and $\hat{y}$ axis are infinite.
2) The two sides of the DSLIM have a symmetric supply. Therefore, the study can be carried out on half motor and results multiplied by two.
3) Air gap δ is constant and slot-less.
4) Stator winding is represented as a sequence of infinite wires along the $\hat{z}$ axis distributed in the air gap, as shown in Fig. 3b. Each wire carries the current $n_{wk}\overline{I}_{0k}$ (current expressed in rms value), where n_{wk} is the number of conductor turns in the kth LIM slot.
5) The reaction rail is homogeneous with constant relative permeability μ_r, permittivity ϵ_{Al}, electrical conductivity σ, and thickness ϵ.
6) The primary has infinite magnetic permeability μ_{fe}. As a consequence, iron saturation is neglected and the superposition principle can be applied[2].
7) The study is performed in steady-state conditions (i.e. in the frequency domain, with phasors).

The model's results are expressed in terms of electromagnetic field distributions, and longitudinal and transverse forces at different slip operating points.

C. Source magnetic vector potential

With reference to Fig. 3b, and similarly to [32], the input source of the model is represented by the algebraic sum of

[2] The hypothesis is justified assuming that the iron core is designed such that the intensity of the magnetic flux density at null speed is below the saturation level of the considered ferromagnetic material (e.g. between 1.5 T and 2.4 T as shown in [33], [34]). At high speed, the intensity of the magnetic flux density decreases.

the magnetic vector potentials generated by each wire in the air gap, in the absence of iron and reaction rail. According to hypotheses 4, 6, 7, and the Biot-Savart law [35], the magnetic vector potential generated by a generic sequence of infinite wires carrying a current phasor $n_{wk}\overline{I}_{0k}$ can be expressed as:

$$A_z^s(x,y) = \sum_k \frac{-n_{wk}\overline{I}_{0k}\mu_0}{2\sqrt{2}\pi} \ln\left(\frac{(x-x_{0k})^2 + (y-y_{0k})^2}{R_{0k}^2}\right) \quad (2)$$

where x_{0k} and y_{0k} are the coordinates of the kth conductor center and R_{0k} its radius. Since each coil comprises two conductors carrying opposite currents, the conductor radius value disappears in the sum, and therefore its value does not matter. According to hypothesis 6, the system is linear, and therefore, the solution of (1) in the air gap can be derived as the sum of the source magnetic potential vector $A_z^s(x,y)$ and the magnetic potential vector resulting from the interaction between the LIM primary and the conducting reaction rail $A_{\delta z}^r(x,y)$. Hence:

$$A_{\delta z}(x,y) = A_z^s(x,y) + A_{\delta z}^r(x,y) \quad (3)$$

D. Solution for the magnetic vector potential

To derive the magnetic vector potential in the primary, air gap, and reaction rail, a resolution method for (1) adapted from [15], [17], [32] for the case of DSLIM, is followed. The solution is obtained through a complex Fourier series decomposition, valid in the interval $x \in [-L/2, L/2]$, where L is the period of the Fourier series. The general solution of (1) is:

$$A_z(x,y) = \sum_{n=-\infty}^{\infty} e^{j\lambda_n x}\left(\beta_n e^{\gamma_n y} + \Gamma_n e^{-\gamma_n y}\right) \quad (4)$$

where $\lambda_n = \frac{2\pi n}{L}$, $\gamma_n = \sqrt{\lambda_n^2 - j\mu\sigma(\omega + v_m\lambda_n)}$, and $\omega = 2\pi f_s$, with f_s being the supply frequency. Depending on the considered region, (4) is re-written accordingly:

1) Primary: electrical conductivity is zero, hence: $\gamma_n = |\lambda_n|$. Moreover, for $y \to \infty$, $A_{\mu z}(x,y) \to 0$, and thus the integration constant β_n has to be 0.
2) Air gap: electrical conductivity is zero, hence: $\gamma_n = |\lambda_n|$. Moreover, as shown in (3), the source magnetic vector potential $A_z^s(x,y)$ has to be added to (4).
3) Reaction rail: the general formulation of (4) is used.

The solution of (1) for the DSLIM of Fig.2 is then the following:

$$\begin{cases} A_{\mu z}(x,y) = \sum_n e^{j\lambda_n x}\Gamma_{\mu n}e^{-|\lambda_n|y} \\ A_{\delta z}(x,y) = A_z^s(x,y) + \sum_n e^{j\lambda_n x}\left(\beta_{\delta n}e^{|\lambda_n|y} + \Gamma_{\delta n}e^{-|\lambda_n|y}\right) \\ A_{\rho z}(x,y) = \sum_n e^{j\lambda_n x}\left(\beta_{\rho n}e^{\gamma_n y} + \Gamma_{\rho n}e^{-\gamma_n y}\right) \end{cases}$$
$$(5)$$

By imposing proper boundary conditions, as described here below, the integration constants $\Gamma_{\mu n}$, $\beta_{\delta n}$, $\Gamma_{\delta n}$, $\beta_{\rho n}$, and $\Gamma_{\rho n}$ are determined.

E. Boundary conditions

At the interface between two media, the following boundary conditions are applied:

- Continuity of the magnetic flux density normal component.
- Continuity of the magnetic field tangential component.

Furthermore, according to hypothesis 2, a symmetry of the magnetic vector potential applies in the middle of the reaction rail. The five equations needed to determine the integration constants are therefore:

$$
\begin{cases}
B_{\mu y}(x, y_{iron}) = B_{\delta y}(x, y_{iron}) \\
\frac{1}{\mu_{fe}} B_{\mu x}(x, y_{iron}) = \frac{1}{\mu_0} B_{\delta x}(x, y_{iron}) \\
B_{\delta y}(x, y_{rail}) = B_{\rho y}(x, y_{rail}) \\
\frac{1}{\mu_0} B_{\delta x}(x, y_{rail}) = \frac{1}{\mu_r} B_{\rho x}(x, y_{rail}) \\
\lim_{y \to 0^+} A_{\rho z}(x, y) = -\lim_{y \to 0^-} A_{\rho z}(x, y)
\end{cases}
\tag{6}
$$

Details on the solution of the boundary conditions are given in the Appendix.

F. Magnetic flux density calculation

By applying $\vec{B} = \vec{\nabla} \times \vec{A}$ to (5), the distribution of the magnetic flux density can be obtained. Of particular interest are the distributions in the air gap and reaction rail. After some development, one obtains:

$$
\begin{cases}
B_{\delta y}(x, y) = B_y^s(x, y) - j \sum_n \lambda_n e^{j\lambda_n x} \left(\beta_{\delta n} e^{|\lambda_n|y} + \Gamma_{\delta n} e^{-|\lambda_n|y} \right) \\
B_{\delta x}(x, y) = B_x^s(x, y) + \sum_n |\lambda_n| e^{j\lambda_n x} \left(\beta_{\delta n} e^{|\lambda_n|y} - \Gamma_{\delta n} e^{-|\lambda_n|y} \right) \\
B_{\rho y}(x, y) = -2j \sum_n \lambda_n e^{j\lambda_n x} \beta_{\rho n} \cosh(\gamma_n y) \\
B_{\rho x}(x, y) = 2 \sum_n \gamma_n e^{j\lambda_n x} \beta_{\rho n} \sinh(\gamma_n y)
\end{cases}
\tag{7}
$$

G. Forces calculation

Once the magnetic vector potential has been derived, the force applied to the reaction rail can be calculated through the integration of Maxwell's stress tensor along the rail surface:

- Longitudinal force (thrust) along the $\hat{\mathbf{x}}$ axis, F_x.
- Transverse (or normal) force along the $\hat{\mathbf{y}}$ axis, F_y

Even though the transverse force cannot be used to generate lift in a DSLIM (contrary to a SLIM), its calculation is of great importance for the optimal design of the mechanical supports of the motor. From the electromagnetic fields, forces can be computed as follows:

$$
F_x = \frac{1}{2\mu_0} \int_{-L/2}^{L/2} \Re\left(B_{\rho x}^*\left(x, \frac{\epsilon}{2}\right) B_{\rho y}\left(x, \frac{\epsilon}{2}\right) \right) dx
\tag{8}
$$

$$
F_y = \frac{1}{4\mu_0} \int_{-L/2}^{L/2} \left(|B_{\rho y}\left(x, \frac{\epsilon}{2}\right)|^2 - |B_{\rho x}\left(x, \frac{\epsilon}{2}\right)|^2 \right) dx
\tag{9}
$$

where the $*$ denotes the complex conjugate, and a factor $\frac{1}{2}$ has to be added to transform the forces from peak to rms values. By substituting (7) into (8) and (9) and after some
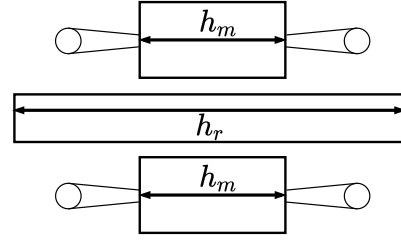

Fig. 4. DSLIM geometry in the **yz** plane. Symmetric primary-rail configuration.

development, the final formulation of the electromagnetic forces for one side of the DSLIM can be obtained:

$$
F_x = 2\Phi \sum_n \Re\left[(\beta_{\rho n} \gamma_n \sinh(\vartheta_n))^* (-j\lambda_n \beta_{\rho n} \cosh(\vartheta_n)) \right]
\tag{10}
$$

$$
F_y = \Phi \sum_n \left(|\lambda_n \beta_{\rho n} \cosh(\vartheta_n)|^2 - |\gamma_n \beta_{\rho n} \sinh(\vartheta_n)|^2 \right)
\tag{11}
$$

where $\Phi = {}^{Lh_m}/\mu_0$, h_m is the primary width along the $\hat{\mathbf{z}}$ axis, and $\vartheta_n = \frac{1}{2} \gamma_n \epsilon$.

H. Slot-less air gap compensation

Since the air gap δ does not have any slots, as stated in hypothesis 3, the air region between primary iron and the reaction rail is smaller than reality. Therefore, the computed forces are overestimated. To compensate for this effect, a correction of the air gap through Carter's coefficient is done, as widely adopted in the literature [5], [13], [21]. With reference to [34], [36], an equivalent air gap δ_e, that takes into account the presence of slots, can be written as:

$$
\delta_e = K_c \delta
\tag{12}
$$

where K_c is Carter's coefficient and can be expressed as [34]:

$$
K_c = \frac{\tau_p}{\tau_p - k b_n}
\tag{13}
$$

where τ_p is the LIM pole pitch, and b_n the slot width. The coefficient k can be written as [34]:

$$
k = \frac{2}{\pi} \left[\arctan\left(\frac{b_n}{2\delta} \right) - \frac{2\delta}{b_n} \ln \sqrt{1 + \left(\frac{b_n}{2\delta} \right)^2} \right]
\tag{14}
$$

I. Edge effect compensation

As described in [36], the effect of the finite width of the motor, and therefore the presence of the so-called "end windings" in the active region of the reaction rail, is called edge effect. In turn, it implies an equivalent decrease in the reaction rail electrical conductivity and can be analyzed through rigorous field analysis. However, in the case of a symmetrical configuration, as depicted in Fig. 4, a correction coefficient for the reaction rail electrical conductivity can be derived, as done in [37] and widely adopted in the literature [5], [36]. The hypotheses used in [37] to derive the correction coefficient are the following:

- The problem is formulated as the relative motion between a magnetic field and a thin reaction rail.

- The thickness of the reaction rail is considerably smaller than the other dimensions.
- The traveling magnetic field varies sinusoidally in both space and time.
- A symmetric primary-rail configuration (see Fig. 4) is used.

With reference to Fig. 4, the so-called Russel-Northworthy factor can be calculated as follows:

$$K_\rho = 1 - \frac{\tanh(\chi)}{\chi \left(1 + \tanh(\chi) \tanh\left(\frac{\pi}{\tau_p}\left(\frac{h_r - h_m}{2}\right)\right)\right)} \quad (15)$$

where h_r is the reaction rail width along the $\hat{\mathbf{z}}$ axis, and $\chi = (\pi h_m)/(2\tau_p)$. Hence, the equivalent reaction rail electrical conductivity σ_e can be calculated as:

$$\sigma_e = K_\rho \sigma \quad (16)$$

Since the width of the primary has a greater impact than the width of the reaction rail on the calculation of the correction factor K_ρ, the hypothesis of symmetrical primary-rail configuration is used in the experimental validation discussed in Section IV.

J. Constant air gap compensation

As stated in hypotheses 1 and 3 (hypotheses necessary for the analytical solution of the magnetic vector potential in the air region), the region at the rear of the primary is made of iron with a constant air gap δ. Because of this assumption, the electromagnetic field magnitude at the rear section of the primary is higher than reality (i.e. case with air behind), as shown in Fig. 1. This effect is called the tail effect and leads to an overestimation of both thrust and normal force developed by the motor. In particular, the overestimation of the normal force is significant, especially at high speed. To overcome this limitation, a compensation of the tail effect based on the integration of the magnetic fields at the rear of the primary is proposed.

The contribution to the overall forces coming from the rear part of the LIM only can be numerically calculated by evaluating the integrals (8) and (9) in the interval $x \in [-L/2, -l_{mot}/2]$, where l_{mot} is the length of the primary. Thanks to the linearity of the model (hypothesis 6), these two contributions can be then subtracted from the overall forces calculated through (10) and (11) for any operating point. Fig. 5 shows the distributions of normal force and thrust along the LIM for a single operating point. The highlighted blue area is the contribution of the rear part only, which is subtracted from the overall force. Although this method neglects the contribution to the overall forces coming from the rear part of the LIM in the case of air behind the primary (because the compensation removes the total contribution of the LIM rear), the numerical and experimental validations prove the validity of the proposed compensation.

IV. MODEL VALIDATION

In order to assess the validity and accuracy of the proposed model, a joint validation through both f.e.m. simulations and
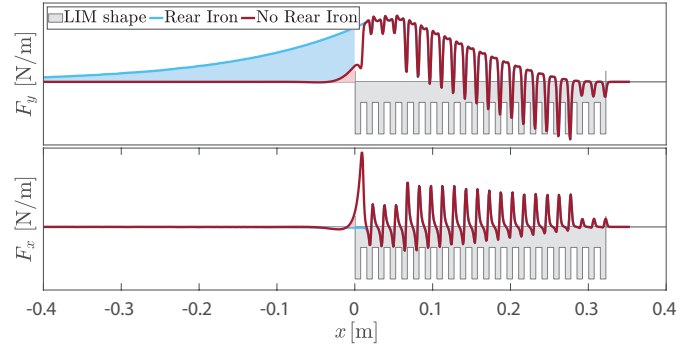

Fig. 5. COMSOL simulations of the distributions of Normal force and thrust for a single operating point ($v_m = 120 \, \mathrm{m \, s^{-1}}$, $f_s = 1323 \, \mathrm{Hz}$). The blue area is the force integral evaluated at the rear section of the LIM which is subtracted from the overall calculations of (10) and (11). The red area is the real force integral evaluated at the rear section of the LIM that is neglected with the proposed compensation method.

measurements via a dedicated test bench is carried out. The DSLIM used for the validation of the model is a 3-pair poles motor whose geometry is reported in Table I[3]. Hereafter, the test bench and the f.e.m. models are described.

A. LIM test bench

A 3D view of the disk-shaped test bench used to experimentally validate the analytical model is shown in Fig. 6, whereas pictures of the real test bench are shown in Fig. 7. The rotating disk has a sandwich structure with a diameter of $1.4 \, \mathrm{m}$. It is composed of a $2 \, \mathrm{mm}$-thick AW-5005 ($\sigma = 30.303 \, \mathrm{MS \, m^{-1}}$) central aluminum disk held together by two $6 \, \mathrm{mm}$-thick AW-6082 ($\sigma = 30.303 \, \mathrm{MS \, m^{-1}}$) aluminum hubs. The electrical conductivity of the disk has been experimentally validated. A curved DSLIM is installed on the bottom of the disk and a

---

[3]The hypothesis of absence of saturation in the primary iron has been validated via COMSOL f.e.m. simulations for the DLSIM prototype geometry and supply current density.
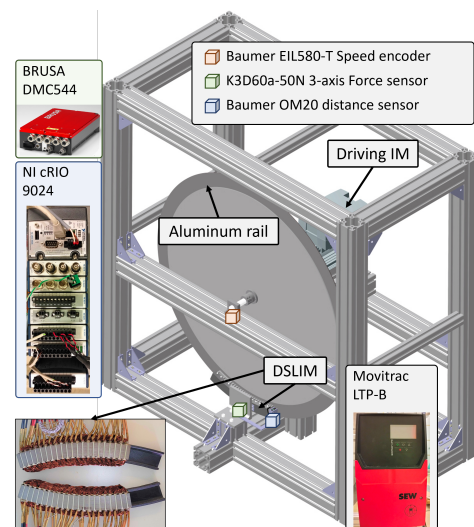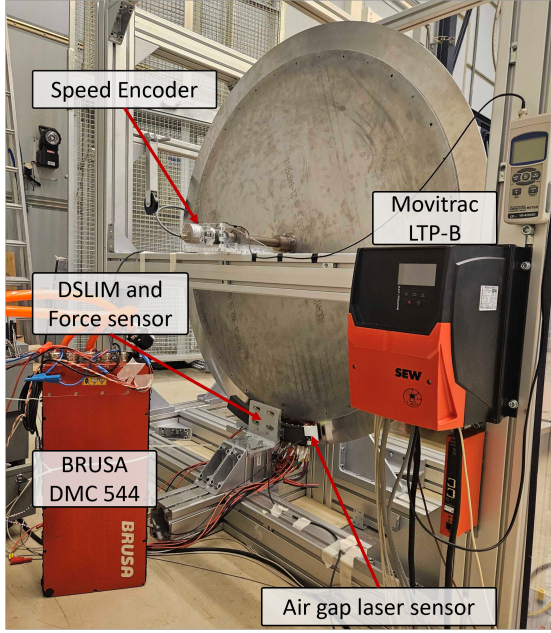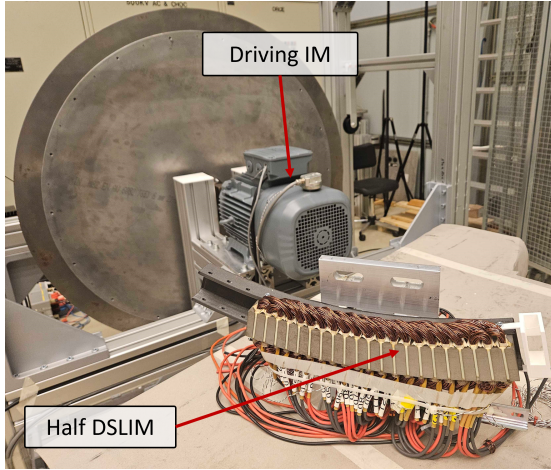

Fig. 6. LIM test bench 3D view.

(a)

(b)

Fig. 7. Pictures of the test bench and DSLIM prototype. (a) Front view with DSLIM installed. (b) Rear view with detail on half the DLSIM prototype.

TABLE I
DSLIM REFERENCE GEOMETRY.

Parameter	Symbol	Value
Pole pitch	τ_p	$0.045\,\mathrm{m}$
Number of pole pairs	p	3
Ratio slot/tooth	α	0.53
Rail thickness	ϵ	$0.002\,\mathrm{m}$
Nominal air gap	δ_n	$0.003\,\mathrm{m}$
Number of slot/pole/phase	$NSPP$	1
Number of turns	N	15
Supply nominal current	I	$10\,\mathrm{Arms}$
Number of phases	m	3
Motor width	h_m	$0.04\,\mathrm{m}$
Motor mass	M	$8\,\mathrm{kg}$

driving induction motor (IM) is mounted on the disk shaft for speed control (obtained through a Voltage Source Inverter Movitrac LTP-B from SEW). The choice of a curved DSLIM

is made for two reasons:

- The curved-primary curved-rail configuration is equivalent to the straight-primary straight-rail configuration in terms of developed forces, as demonstrated in [38] via f.e.m. simulations.
- As experimentally demonstrated in [39], contrary to the straight-primary straight-rail configuration, a straight-primary curved-rail configuration induces eddy currents in the reaction rail at synchronous speed and, therefore, generates forces that do not exist in the real configuration.

The bench is equipped with a 3-axis force sensor (K3D60a-50N from Meßsysteme) to measure the LIM force components, a National Instruments CompactRIO 9024 used to control the driving IM and to acquire sensor data, an optical speed encoder (EIL580-T from Baumer) to measure the disk rotation speed, and a laser distance sensor (OM20 RS485 from Baumer) to measure the air gap. The supply of the DSLIM is obtained through a BRUSA DMC-544 voltage source inverter supplied by a DC power source. Tables II and III list the installed sensors and actuators with their measuring ranges and accuracies. Different air gap values can be set on the bench, starting from a minimum value of $3\,\mathrm{mm}$. The air gap can be adjusted according to the procedure described in algorithm 1.

TABLE II
TEST BENCH SENSOR SPECIFICATIONS.

Sensor	Range	Accuracy	Description
K3D60a-50N	$\pm 50\,\mathrm{N}$	0.5%	3-axis force meas.
OM20 RS485	$10\,\mathrm{mm}$	$1\,\mathrm{\mu m}$	Air gap meas.
EIL580-T	$3000\,\mathrm{rpm}$	0.072°	Disk rotation speed encoder

TABLE III
TEST BENCH ACTUATORS.

Actuator and output	Type	Description
NI 9263	Analog OUT	IM speed set point
NI 9474	Digital IO	IM drive enable
Movitrac LTP-B	Voltage Source Inverter	IM drive
BRUSA DMC544	Voltage Source Inverter	DSLIM drive

B. COMSOL model

A finite element 2D model has been developed in COMSOL Multiphysics for the numerical validation of the proposed analytical model. In this respect, as formulated in [40], the magnetic fields (mf) interface of the AC/DC COMSOL module has been used to numerically solve Poisson's equation for the magnetic vector potential in the frequency domain. To account for the speed of the LIM, the Lorentz term (i.e. velocity term) has been added to the current density formulation in the stator [41]. The model mesh is mainly made of triangles and quads, with 88000 elements and an average skewness element quality of 0.899. The skewness is the default quality measure in COMSOL and it is a measure of the equiangular skew of the mesh elements. According to [42], it is defined as the minimum of the following quantity:

$$S_k = 1 - \max\left(\frac{\theta - \theta_e}{180 - \theta_e}, \frac{\theta_e - \theta}{\theta_e}\right)$$

Algorithm 1 Air gap adjustment

1: Unscrew the LIM sliding support.
2: Slide the LIM against the reaction rail until the primary touches the disk. The air gap is now $0\,\mathrm{mm}$.
3: Set the zero position of the laser distance sensor.
4: Slide the LIM to the desired air gap with the aid of calibrated steel spacers.
5: Fix the LIM sliding support.
6: Spin the disk through the driving IM at low speed (e.g. $20\,\mathrm{rpm} \simeq 1.5\,\mathrm{m\,s^{-1}}$).
7: Measure the air gap through the laser distance sensor and verify it corresponds to the nominal set value δ_n plus the tolerance margin.
8: **if** $\delta_n - 0.5\,\mathrm{mm} \leq \delta \leq \delta_n + 0.5\,\mathrm{mm}$ **then**
9:     The procedure is complete.
10: **else**
11:     Unscrew the LIM sliding support.
12:     Repeat procedure from point 4.
13: **end if**

---

where θ is the angle over a vertex, θ_e is the angle of the corresponding vertex in an ideal element, and the minimum is taken on all vertices of the element. The simulations are carried out on the following machine:

- Laptop: Lenovo ThinkPad X1 Carbon Gen 9
- Processor: 11th Gen Intel(R) Core(TM) $i7 - 1185G7$ $3\,\mathrm{GHz}$, 4 cores
- Installed Memory RAM: $32\,\mathrm{GB}$

C. Key Performance Indicators

The results comparison between the proposed analytical model, the f.e.m. model, and the measurements is done by comparing the longitudinal and transverse forces for different operating points (i.e. slip points). In the following figures, multiple curves are represented. Every curve represents a force component as a function of the LIM velocity for a constant supply frequency. The comparison relies on the following metrics:

- Maximum error to capture the highest difference between the results of the proposed LIM model versus the f.e.m. benchmark and the experimental results.
- RMS error to quantify the average quality of the results produced by the proposed LIM model versus the f.e.m. benchmark and the experimental results. The RMSE is computed as follows: $RMSE = \sqrt{\frac{\sum_i^N \left(X_i - \hat{X}_i\right)^2}{N}}$

The maximum value of the forces at each supply frequency has been used as a base for the normalization of the errors. In what follows, the numerical and experimental validations are treated separately for the sake of clarity.

D. Validation via f.e.m. COMSOL

Fig. 8 shows the comparison in terms of longitudinal force (thrust) and normal force between the proposed analytical model and the f.e.m. COMSOL model, whereas Fig. 9 shows the maximum and RMS errors of the forces at each simulated

frequency. Since the COMSOL model used as a benchmark is bi-dimensional, the compensation of the edge effect, as presented in Section III-I, is not applied. Therefore, the proposed analytical model is reduced to its bi-dimensional formulation (i.e. $K_\rho = 1$). As shown in Fig. 8, the proposed analytical model exhibits excellent accuracy throughout the whole speed range for both force components. With respect to Fig. 9, one can further notice the following:

- Maximum and RMS errors are bounded in every simulation.
- RMS error, which is the most relevant metric for LIM models performance computation, is of few % and bounded to less than 3%.

Moreover, the simulation times of the analytical model and COMSOL f.e.m. are reported in Table IV. As shown in the table, one of the greatest advantages of the proposed analytical model is its computation efficiency, which makes it possible to be integrated into an optimization framework during the design phase, whereas an f.e.m.-based optimization would require much longer execution times and therefore be impractical. Indeed, thanks to the computation efficiency of the proposed model, a brute-force approach can be used to derive an optimal LIM design in a short time by performing a parametric sweep of the main design parameters (e.g. p, τ_p, ϵ, $NSPP$, h_m ...). The validation of the proposed analytical model has also been carried out in terms of magnetic flux density distributions. Fig. 10 shows the magnetic flux density distributions at the primary and rail surfaces (i.e. $y = \delta + \frac{\epsilon}{2}$ and $y = \frac{\epsilon}{2}$ respectively) for a single operating point, computed via the proposed analytical model and COMSOL f.e.m.. As can be noticed, the fields computed through the proposed analytical model match the f.e.m. fields with excellent accuracy in the primary region. As expected, however, the fields computed via the analytical model are overestimated at the rear of the primary. This overestimation is due to hypotheses 1 and 3 (i.e. constant air gap throughout the entire Fourier series period), whose effect on the forces (i.e. the tail effect) has been discussed in Section III-J, and a method to compensate for it has been proposed.

TABLE IV
COMPARISON OF THE COMPUTATION TIMES FOR A DIFFERENT NUMBER OF SUPPLY FREQUENCIES.

Simulation type	Analytical	COMSOL
Single supply frequency	$3.3\,\mathrm{s}$	$\simeq 0.5\,\mathrm{h}$
Full characteristic (15 frequencies)	$25\,\mathrm{s}$	$\simeq 3\,\mathrm{h}$

E. Validation via experimental measurements

Regarding the experimental validation of the proposed analytical model, the following aspects have to be considered.

- The finite width of the DSLIM is taken into account through the edge effect compensation presented in Section III-I. This produces an equivalent increase of the reaction rail resistivity of 55% if applied to the bench geometry.
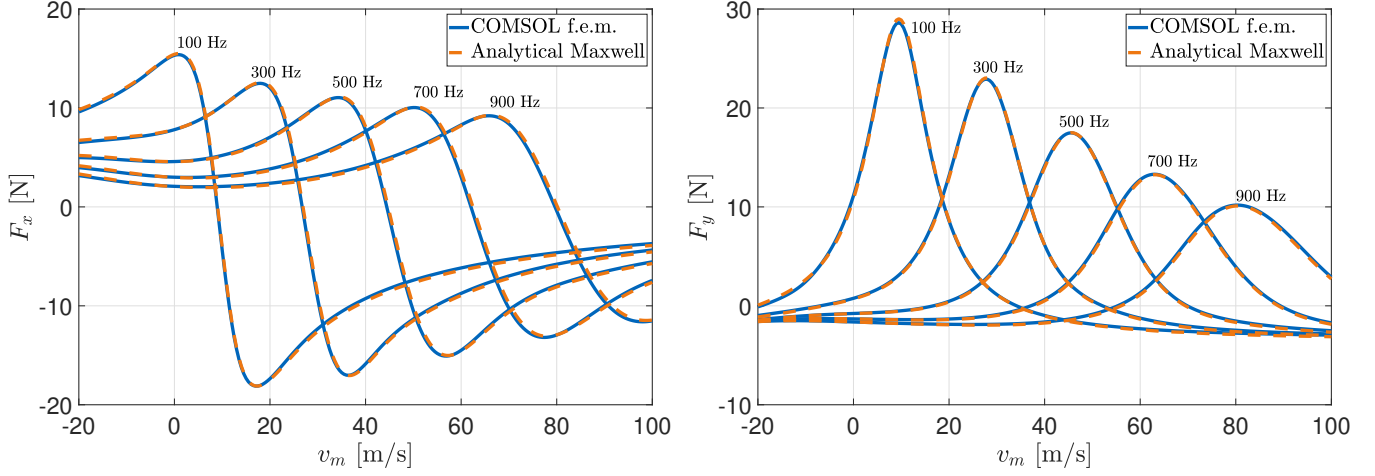
Fig. 8. Longitudinal force F_x and normal force F_y comparisons between analytical model and COMSOL f.e.m. simulations.
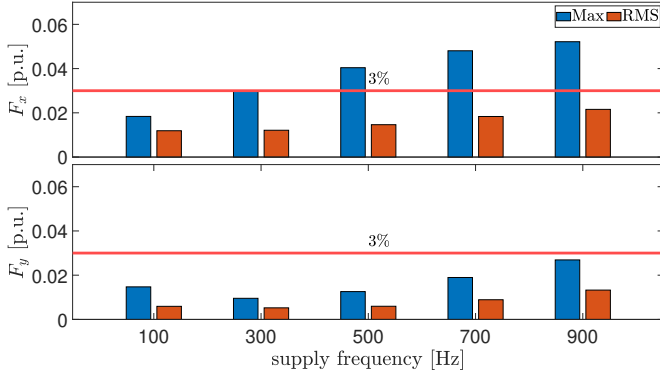

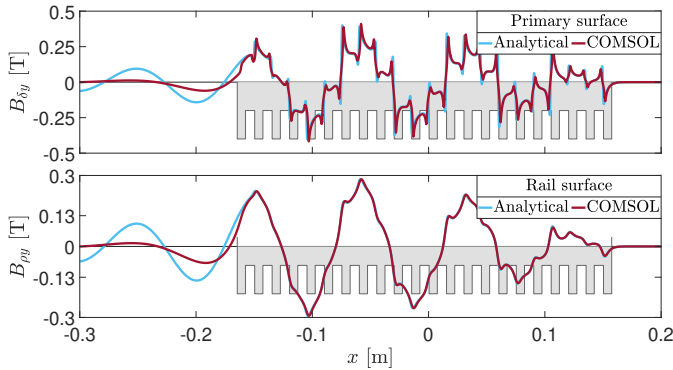Fig. 9. Maximum and RMS errors between the analytical model and COMSOL f.e.m. simulations.

Fig. 10. Magnetic flux density y component distribution at the primary and reaction rail surfaces. $v_m = 50\,\mathrm{m\,s}^{-1}$, $f_s = 500\,\mathrm{Hz}$. Comparison between the proposed analytical model (blue) and COMSOL f.e.m. (red).

- Due to the irregularities of the 2mm-thick disk used as reaction rail, the air gap cannot be guaranteed to be constant. To overcome this issue, particularly relevant at low speed, the analytical model simulations are computed using an air gap interval centered around the nominal

value (i.e. $\delta = \delta_n \pm 0.5\,\mathrm{mm}$). This $\pm 0.5\,\mathrm{mm}$ interval has been measured via the laser sensor listed in Table II. The interval is represented by the shaded areas in the result figures.

- The measurements are carried out at 5 different supply frequencies, with $f_s = 900\,\mathrm{Hz}$ being the highest frequency the BRUSA DMC544 is capable of supplying.

- Because of the limitations of the BRUSA DMC544, the nominal current of $10A_{rms}$ has been lowered to $7A_{rms}$ for $f_s \geq 700\,\mathrm{Hz}$.

- Measurements are bounded at speeds around the synchronous one because the DC source used to supply the BRUSA DMC544 is not bi-directional (i.e. the max speed reached at each supply frequency is such that the DC bus power flow is not reverted).

- Every measurement point is the average over $10\,\mathrm{s}$ of forces acquisition, corresponding to 8300 raw samples.

Fig. 11 shows the comparison between the measurements and the proposed analytical model results with a nominal air gap of $3\,\mathrm{mm}$. As can be seen, the measurements accurately follow the results of the analytical model, especially in the proximity of the synchronous speed, which is the highest-efficiency working region (as known from classic induction machines theory). Furthermore, to extend the model validity for different configurations, the comparison has been carried out with a larger air gap (i.e. $\delta_n = 4\,\mathrm{mm}$). Results are consistent with the case of $\delta_n = 3\,\mathrm{mm}$, and can be seen in Fig. 12. Fig. 13 and Fig. 14 show the maximum and RMS errors of the forces at each measured supply frequency in the case of $\delta_n = 3\,\mathrm{mm}$ and $\delta_n = 4\,\mathrm{mm}$ respectively. From the error figures, one can notice the following:

- Maximum and RMS errors are bounded in every simulation.

- RMS error, which is the most relevant metric for LIM models performance computation, is of few % and bounded to less than 10%.
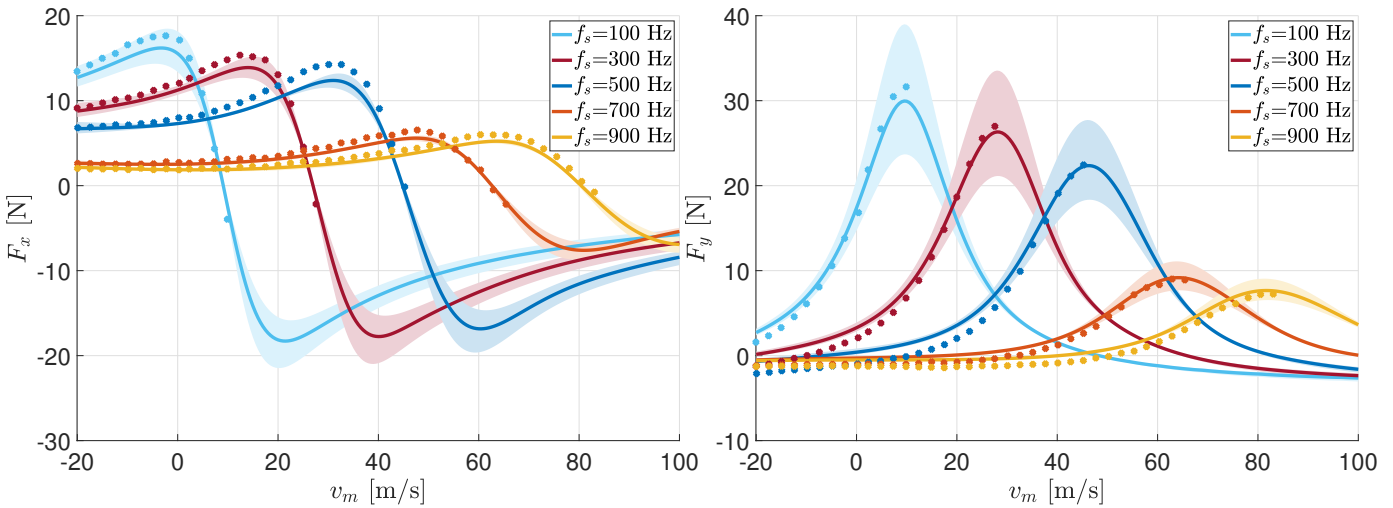
Fig. 11. Longitudinal force F_x and normal force F_y comparisons between measurements (dots) and the proposed analytical model (solid) with $\delta_n = 3\,\mathrm{mm}$. The shaded areas represent the air gap interval used in the simulations.
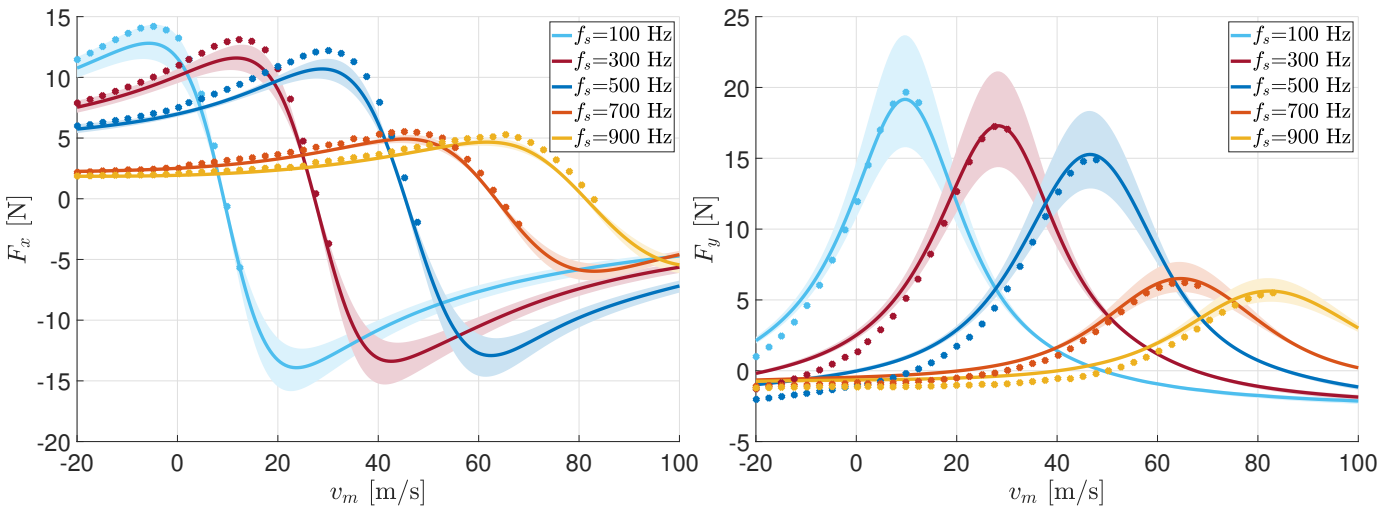

Fig. 12. Longitudinal force F_x and normal force F_y comparisons between measurements (dots) and the proposed analytical model (solid) with $\delta_n = 4\,\mathrm{mm}$. The shaded areas represent the air gap interval used in the simulations.
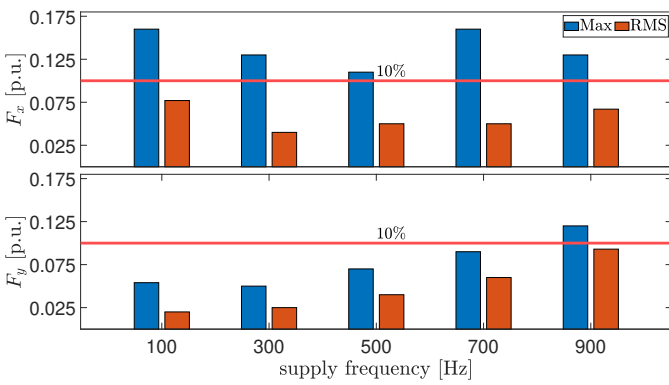

Fig. 13. Maximum and RMS errors between the analytical model and experimental measurements with $\delta_n = 3\,\mathrm{mm}$.
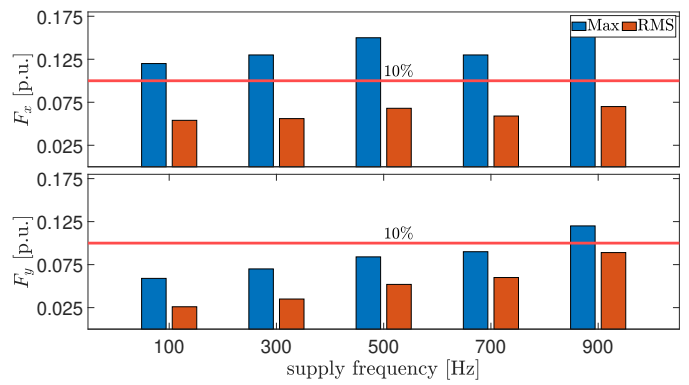

Fig. 14. Maximum and RMS errors between the analytical model and experimental measurements with $\delta_n = 4\,\mathrm{mm}$.

V. CONCLUSION

In this paper, a computationally efficient pseudo-three-dimensional model of a DSLIM, based on a Fourier series decomposition method, has been proposed and its results validated through both COMSOL f.e.m. models and experimental

results obtained with a dedicated test bench. The proposed model explicitly considers the main characteristics of DSLIMs (i.e. end effect, edge effect, slot effect, mmf space harmonics, and tail effect), and is computationally efficient and very accurate up to high speed (i.e. $v \simeq 100\,\mathrm{m\,s^{-1}}$). Indeed, the comparison of the simulated forces with COMSOL f.e.m. models has shown that maximum and RMS errors are always bounded and that the RMS error is of few % and bounded to 3%. Experimental results also confirmed the accuracy and fidelity of the proposed analytical model throughout the whole speed range of interest, with a maximum RMS error of 9%. Moreover, the greatest advantage of the proposed analytical model is its computation efficiency, which makes it possible to be integrated into an optimization framework during the design phase of the LIMs.

APPENDIX
BOUNDARY CONDITIONS SOLUTION

A resolution approach similar to what is done in [17] and [32] is followed to solve the system of equations in (6). By recalling that $\vec{B} = \vec{\nabla} \times \vec{A}$ and inserting (5) into the boundary conditions system of equations, (6) becomes:

$$
\begin{cases}
B_{yna}^s = -j\lambda_n \Gamma_{\mu n} e^{-|\lambda_n|a} + j\lambda_n \left(\beta_{\delta n} e^{|\lambda_n|a} + \Gamma_{\delta n} e^{-|\lambda_n|a}\right) \\
B_{xna}^s = -|\lambda_n| \left(\beta_{\delta n} e^{|\lambda_n|a} - \Gamma_{\delta n} e^{-|\lambda_n|a}\right) \\
B_{yn\epsilon}^s = j\lambda_n \left(\beta_{\delta n} e^{|\lambda_n|\frac{\epsilon}{2}} + \Gamma_{\delta n} e^{-|\lambda_n|\frac{\epsilon}{2}}\right) - 2j\lambda_n \beta_{\rho n} \cosh(\vartheta_n) \\
B_{xn\epsilon}^s = -|\lambda_n| \left(\beta_{\delta n} e^{|\lambda_n|\frac{\epsilon}{2}} - \Gamma_{\delta n} e^{-|\lambda_n|\frac{\epsilon}{2}}\right) + \frac{2\gamma_n}{\mu_r} \beta_{\rho n} \sinh(\vartheta_n) \\
\beta_{\rho n} = \Gamma_{\rho n}
\end{cases}
\tag{17}
$$

where $a = \frac{\epsilon}{2} + \delta$. Similarly to [32], the Kronecker delta operator (δ_{nm}) has been used to remove the x exponential in the magnetic vector potential formulation of (5) and therefore simplify the boundary condition equations.

$$
\delta_{nm} = \frac{1}{L} \int_{-\frac{L}{2}}^{\frac{L}{2}} e^{(-j\lambda_m x)} e^{(j\lambda_n x)} dx
\tag{18}
$$

Moreover, since (17) has to be satisfied for each harmonic index n, the sum $\sum_n$ can be removed. As a consequence of the above-mentioned simplification, the Fourier series coefficients of the x and y components of the magnetic flux density field due to the source $\vec{B}^s(x,y) = \vec{\nabla} \times A_z^s(x,y)$ have to be calculated:

$$
B_{yna}^s = \frac{1}{L} \int_{-\frac{L}{2}}^{\frac{L}{2}} -\left.\frac{\partial A_z^s(x,y)}{\partial x}\right|_{y=a} e^{(-j\lambda_n x)} dx
\tag{19}
$$

$$
B_{xna}^s = \frac{1}{L} \int_{-\frac{L}{2}}^{\frac{L}{2}} \left.\frac{\partial A_z^s(x,y)}{\partial y}\right|_{y=a} e^{(-j\lambda_n x)} dx
\tag{20}
$$

$$
B_{yn\epsilon}^s = \frac{1}{L} \int_{-\frac{L}{2}}^{\frac{L}{2}} -\left.\frac{\partial A_z^s(x,y)}{\partial x}\right|_{y=\frac{\epsilon}{2}} e^{(-j\lambda_n x)} dx
\tag{21}
$$

$$
B_{xn\epsilon}^s = \frac{1}{L} \int_{-\frac{L}{2}}^{\frac{L}{2}} \left.\frac{\partial A_z^s(x,y)}{\partial y}\right|_{y=\frac{\epsilon}{2}} e^{(-j\lambda_n x)} dx
\tag{22}
$$

The system of equations (17) can be solved by numerically evaluating the above integrals through a calculation tool such as Matlab, or Mathematica. For the scope of this paper, only the integration constants $\beta_{\delta n}$, $\Gamma_{\delta n}$, and $\beta_{\rho n}$ are of interest (as they are the only one appearing in the fields and force formulations (7), (10), and (11)). Their expressions are the following:

$$
\beta_{\delta n} = -\frac{\lambda_n |\lambda_n| \cosh(\vartheta_n) \left(e^{a|\lambda_n|} B_{xna}^s - e^{\frac{\epsilon}{2}|\lambda_n|} B_{xn\epsilon}^s\right)}{D_{n1}} \\
- \frac{\gamma_n \sinh(\vartheta_n) \left(e^{a|\lambda_n|} \lambda_n B_{xna}^s + je^{\frac{\epsilon}{2}|\lambda_n|} |\lambda_n| B_{yn\epsilon}^s\right)}{D_{n1}}
\tag{23}
$$

$$
\Gamma_{\delta n} = -D_{n2} \lambda_n |\lambda_n| \cosh(\vartheta_n) \left(e^{\frac{\epsilon}{2}|\lambda_n|} B_{xna}^s - e^{a|\lambda_n|} B_{xn\epsilon}^s\right) \\
+ D_{n2} \gamma_n \sinh(\vartheta_n) \left(e^{\frac{\epsilon}{2}|\lambda_n|} \lambda_n B_{xna}^s - je^{a|\lambda_n|} |\lambda_n| B_{yn\epsilon}^s\right)
\tag{24}
$$

$$
\beta_{\rho n} = \frac{\operatorname{csch}(\vartheta_n)}{D_{n3}} \\
\left(-2e^{\left(a+\frac{\epsilon}{2}\right)\lambda_n} B_{xna}^s + e^{2a\lambda_n} \hat{B}_{n\epsilon}^s + e^{\epsilon\lambda_n} \hat{B}_{n\epsilon}^{s*}\right)
\tag{25}
$$

where $\hat{B}_{n\epsilon}^s = B_{xn\epsilon}^s + jB_{yn\epsilon}^s$, and:

$$
D_{n1} = \lambda_n |\lambda_n| \left(e^{2a|\lambda_n|} - e^{\epsilon|\lambda_n|}\right) |\lambda_n| \cosh(\vartheta_n) + \\
\lambda_n |\lambda_n| \left(e^{2a|\lambda_n|} + e^{\epsilon|\lambda_n|}\right) \gamma_n \sinh(\vartheta_n)
$$

$$
D_{n2} = \frac{e^{\left(a+\frac{\epsilon}{2}\right)|\lambda_n|}}{D_{n1}}
$$

$$
D_{n3} = 2e^{\epsilon\lambda_n} \left(\gamma_n - \lambda_n \coth(\vartheta_n)\right) + \\
2e^{2a\lambda_n} \left(\gamma_n + \lambda_n \coth(\vartheta_n)\right)
$$

REFERENCES

[1] I. Boldea and S. Nasar, "Linear electric actuators and generators," *IEEE Transactions on Energy Conversion*, vol. 14, no. 3, pp. 712–717, Sep. 1999.

[2] E. Laithwaite and F. Barwell, "Linear induction motors for high-speed railways," *Electronics and Power*, vol. 10, no. 4, pp. 100–103, Apr. 1964.

[3] R. Hellinger and P. Mnich, "Linear Motor-Powered Transportation: History, Present Status, and Future Outlook," *Proceedings of the IEEE*, vol. 97, no. 11, pp. 1892–1900, Nov. 2009.

[4] T. C. Wang, "Linear Induction Motor for High-Speed Ground Transportation," *IEEE Transactions on Industry and General Applications*, vol. IGA-7, no. 5, pp. 632–642, Sep. 1971.

[5] S. E. Abdollahi, M. Mirzayee, and M. Mirsalim, "Design and Analysis of a Double-Sided Linear Induction Motor for Transportation," *IEEE Transactions on Magnetics*, vol. 51, no. 7, pp. 1–7, Jul. 2015.

[6] T. Higuchi, S. Nonaka, and M. Ando, "On the design of high-efficiency linear induction motors for linear metro," *Electrical Engineering in Japan*, vol. 137, no. 2, pp. 36–43, 2001.

[7] R. Palka and K. Woronowicz, "Linear Induction Motors in Transportation Systems," *Energies*, vol. 14, no. 9, p. 2549, Jan. 2021.

[8] K. Woronowicz and A. Safaee, "Linear motor drives and applications in rapid transit systems," in *2014 IEEE Transportation Electrification Conference and Expo (ITEC)*. Dearborn, MI, USA: IEEE, Jun. 2014, pp. 1–96.

[9] P. E. Ross, "Hyperloop: No pressure," *IEEE Spectrum*, vol. 53, no. 1, pp. 51–54, Jan. 2016.

[10] A. Cassat, V. Bourquin', M. Badoux, D. Vernez, and M. JuferdeN, "SWISSMETRO - ProjectDevelopment Status," *Internatienal Symposium on Speed-up and ServiceTechnology for Rail and Maglev Systems*, p. 8, 2003.

[11] D. Tudor and M. Paolone, "Operational-Driven Optimal-Design of a Hyperloop System," *Transportation Engineering*, p. 100079, Jun. 2021.

[12] H. Almujibah, S. I. Kaduk, and J. Preston, "Hyperloop – prediction of social and physiological costs," *Transportation Systems and Technology*, vol. 6, no. 3, pp. 43–59, Sep. 2020.

[13] A. Shiri and A. Shoulaie, "Design Optimization and Analysis of Single-Sided Linear Induction Motor, Considering All Phenomena," *IEEE Transactions on Energy Conversion*, vol. 27, no. 2, pp. 516–525, Jun. 2012.

[14] J. Gieras, G. Dawson, and A. Eastham, "Performance calculation for single-sided linear induction motors with a double-layer reaction rail under constant current excitation," *IEEE Transactions on Magnetics*, vol. 22, no. 1, pp. 54–62, Jan. 1986.

[15] M. Abdelqader, J. Morelli, R. Palka, and K. Woronowicz, "2-D quasi-static fourier series solution for a single coil of a linear induction motor," in *2016 IEEE Conference on Electromagnetic Field Computation (CEFC)*, Nov. 2016, pp. 1–1.

[16] A. Shiri, "Electromagnetic force analysis in linear induction motors, considering end effect," in *2016 7th Power Electronics and Drive Systems Technologies Conference (PEDSTC)*, Feb. 2016, pp. 105–110.

[17] K. Woronowicz, M. Abdelqader, R. Palka, and J. Morelli, "2-D quasi-static Fourier series solution for a linear induction motor," *COMPEL - The international journal for computation and mathematics in electrical and electronic engineering*, vol. 37, no. 3, pp. 1099–1109, Jan. 2018.

[18] S. Yamamura, H. Ito, and Y. Ishulawa, "Theories of the Linear, Induction Motor and Compensated Linear Induction Motor," *IEEE Transactions on Power Apparatus and Systems*, vol. PAS-91, no. 4, pp. 1700–1710, Jul. 1972.

[19] M. Iwamoto, E. Ohno, T. Itoh, and Y. Shinryo, "End-Effect of High-Speed Linear Induction Motor," *IEEE Transactions on Industry Applications*, vol. IA-9, no. 6, pp. 632–639, Nov. 1973.

[20] E. A. Mendrela and E. Gierczak, "Two-dimensional analysis of linear induction motor using Fourier's series method," *Archiv fur Elektrotechnik*, vol. 65, no. 1-2, pp. 97–106, Jan. 1982.

[21] F. Carter, "The magnetic field of the dynamo-electric machine," *Journal of the Institution of Electrical Engineers*, vol. 64, no. 359, pp. 1115–1138, Nov. 1926.

[22] T. Yamaguchi, Y. Kawase, M. Yoshida, Y. Saito, and Y. Ohdachi, "3-D finite element analysis of a linear induction motor," *IEEE Transactions on Magnetics*, vol. 37, no. 5, pp. 3668–3671, Sep. 2001.

[23] E. Amiri and E. A. Mendrela, "A Novel Equivalent Circuit Model of Linear Induction Motors Considering Static and Dynamic End Effects," *IEEE Transactions on Magnetics*, vol. 50, no. 3, pp. 120–128, Mar. 2014.

[24] Y. Zhang, M. Zhang, W. Ma, J. Xu, J. Lu, and Z. Sun, "Modeling of a Double-stator Linear Induction Motor," *IEEE Transactions on Energy Conversion*, vol. 27, no. 3, pp. 572–579, Sep. 2012.

[25] T. Mishima, M. Hiraoka, and T. Nomura, "A study of the optimum stator winding arrangement of LIM in maglev systems," in *IEEE International Conference on Electric Machines and Drives, 2005.*, May 2005, pp. 1238–1242.

[26] J. Duncan, "Linear induction motor-equivalent-circuit model," *IEE Proceedings B (Electric Power Applications)*, vol. 130, no. 1, pp. 51–57, Jan. 1983.

[27] K. Woronowicz and A. Safaee, "A novel linear induction motor equivalent-circuit with optimized end effect model," *Canadian Journal of Electrical and Computer Engineering*, vol. 37, no. 1, pp. 34–41, 2014.

[28] W. Xu, J. G. Zhu, Y. Zhang, Z. Li, Y. Li, Y. Wang, Y. Guo, and Y. Li, "Equivalent Circuits for Single-Sided Linear Induction Motors," *IEEE Transactions on Industry Applications*, vol. 46, no. 6, pp. 2410–2423, Nov. 2010.

[29] M. Amrhein and P. T. Krein, "Induction Machine Modeling Approach Based on 3-D Magnetic Equivalent Circuit Framework," *IEEE Transactions on Energy Conversion*, vol. 25, no. 2, pp. 339–347, Jun. 2010.

[30] A. Fatima, T. Stachl, W. Li, M. S. Toulabi, G. Byczynski, J. Tjong, and N. C. Kar, "Electromagnetic Performance Prediction of an Induction Machine Using an Improved Permeance-Based Equivalent Circuit Model Considering the Frequency and B–H Curve Dependent Core Loss Branches," *IEEE Transactions on Industry Applications*, vol. 59, no. 2, pp. 1283–1294, Mar. 2023.

[31] S. Yamamura and H. Ito, "Three-dimensional analysis of linear induction motors," *Electrical Engineering in Japan*, vol. 96, no. 2, pp. 55–61, 1976.

[32] M. Abdelqader, J. Morelli, R. Palka, and K. Woronowicz, "2-D quasi-static solution of a coil in relative motion to a conducting plate," *COMPEL - The international journal for computation and mathematics in electrical and electronic engineering*, vol. 36, no. 4, pp. 980–990, Jan. 2017.

[33] M. A. Prabhu, J. Y. Loh, S. C. Joshi, V. Viswanathan, S. Ramakrishna, C. J. Gajanayake, and A. K. Gupta, "Magnetic Loading of Soft Magnetic Material Selection Implications for Embedded Machines in More Electric Engines," *IEEE Transactions on Magnetics*, vol. 52, no. 5, pp. 1–6, May 2016.

[34] J. Pyrhonen, T. Jokinen, and V. Hrabovcová, *Design of rotating electrical machines*. Chichester, West Sussex, United Kingdom ; Hoboken, NJ: Wiley, 2008.

[35] T. Charitat and F. Graner, "About the magnetic field of a finite wire," *European Journal of Physics*, vol. 24, no. 3, p. 267, Mar. 2003.

[36] I. Boldea, *Linear Electric Machines, Drives, and MAGLEVs Handbook*, 1st ed. CRC Press, Dec. 2017.

[37] R. L. Russell and K. H. Norsworthy, "Eddy currents and wall losses in screened-rotor induction motors," *Proceedings of the IEE - Part A: Power Engineering*, vol. 105, no. 20, pp. 163–175, Apr. 1958.

[38] J. A. Pochon, "Design and build of a test bench for the characterisation of a Linear Induction Motor (LIM) applied to a hyperloop propulsion system Master's thesis 2022," École Polytechnique Fédérale de Lausanne, Tech. Rep., Jun. 2022.

[39] Y. Kotani, T. Morizane, K. Tsujikawa, N. Kimura, and H. Omori, "The dynamic characteristics of LIM using disc-shaped secondary side converted into linear motion," in *2012 15th International Conference on Electrical Machines and Systems (ICEMS)*, Oct. 2012, pp. 1–6.

[40] J.-M. Jin, "Chapter 4: Two-Dimensional Finite Element Analysis," in *The finite element method in electromagnetics*, 3rd ed. Hoboken. New Jersey: John Wiley & Sons Inc, 2014.

[41] COMSOL, "Software for Simulating Static and Low-Frequency Electromagnetics," 2023, https://www.comsol.com/acdc-module.

[42] Comsol, "Mesh Element Quality," 2021, https://www.comsol.com/blogs/how-to-inspect-your-mesh-in-comsol-multiphysics.